Monthly Notices of the ROYAL ASTRONOMICAL SOCIETY

MNRAS **516,** 5989–5996 (2022) https://doi.org/10.1093/mnras/stac2545
Advance Access publication 2022 September 9

Two-spacecraft detection of short-period decayless kink oscillations of solar coronal loops

Sihui Zhong [1]★ Valery M. Nakariakov,[1,2]★ Dmitrii Y. Kolotkov [1]★ Cis Verbeeck[3] and David Berghmans[3]

[1]*Centre for Fusion, Space and Astrophysics, Department of Physics, University of Warwick, Coventry CV4 7AL, UK*
[2]*Centro de Investigacion en Astronomía, Universidad Bernardo O'Higgins, Avenida Viel 1497, Santiago, Chile*
[3]*Solar-Terrestrial Centre of Excellence – SIDC, Royal Observatory of Belgium, Ringlaan – 3 – Avenue Circulaire, B-1180 Brussels, Belgium*

Accepted 2022 September 5. Received 2022 September 2; in original form 2022 July 29

ABSTRACT

Decayless kink oscillations of an ensemble of loops are captured simultaneously by the High Resolution Imager (HRI) of the Extreme Ultraviolet Imager (EUI) and the Atmospheric Imaging Assembly (AIA) from 22:58 UT on 2021 November 5 to 00:27 UT on 2021 November 6. Oscillations are analysed by processing image sequences taken by the two instruments with a motion magnification technique. The analysed loops are around 51 Mm in length, and oscillate with short periods of 1–3 min (1.6 min in average) and displacement amplitudes of 24–83 km. The signals recorded by AIA are delayed by 66 s as compared to HRI, which coincides with the light traveltime difference from the Sun to each instrument. After correction of this time difference, the cross-correlation coefficient between the signals from the two data varies from 0.82 to 0.97, indicating that they are well consistent. This work confirms that HRI sees the same oscillations as AIA, which is the necessary first step before proceeding to the detection of shorter time-scales by EUI. In addition, our results indicate the robustness of the dejittering procedure in the study of kink oscillations with HRI.

Key words: waves – Sun: corona – Sun: oscillations.

1 INTRODUCTION

Oscillatory and wave phenomena detected in the solar corona are subject to intensive study mainly in the context of their possible relevance to the long-standing problem of coronal plasma heating (e.g. Van Doorsselaere et al. 2020) and because of their plasma diagnostics potential (e.g. Nakariakov et al. 2021). A puzzling class of coronal oscillations is the omnipresent low-amplitude decayless kink oscillations of coronal loops, appearing as repetitive displacements of the loops in the plane of the sky (Wang et al. 2012) or as persistent Doppler shift oscillations of coronal emission lines (Tian et al. 2012). The oscillation periods have been found to range from 1.5 to 10 min, and scale linearly with the loop length (Anfinogentov, Nakariakov & Nisticò 2015). The latter finding indicates that the oscillations are standing kink modes. The average apparent displacement amplitude in the plane of the sky is 0.17 Mm, i.e. smaller than the pixel size of available coronal extreme ultraviolet (EUV) imagers.

The main interest in decayless kink oscillations is connected with their ubiquity. In particular, the oscillations are seen to occur without any association with energy releases such as flows or eruptions. It allows one to use them for seismological diagnostics of coronal loops and active regions during quiet times (Anfinogentov & Nakariakov 2019), i.e. before flares and eruptions. The simultaneous detection of the fundamental and second parallel (axial) harmonics (Duckenfield et al. 2018) opened up a possibility to study the field-aligned structure of the equilibrium plasma parameters in the oscillating loop (e.g. Andries, Arregui & Goossens 2005; Andries et al. 2009). In addition, revealing the mechanism for the compensation of the oscillation damping may shed light on the energy balance in active regions.

Several mechanisms responsible for the existence of decayless kink oscillations have been proposed. Nakariakov et al. (2016) ruled out their excitation by monochromatic drivers such as p-modes or chromospheric oscillations. Concerning non-monochromatic mechanisms, it has been proposed that the energy could come from slowly varying flows by the self-oscillatory mechanism (Nakariakov et al. 2016; Karampelas & Van Doorsselaere 2020), or the Alfvénic vortex shedding (Nakariakov, Aschwanden & van Doorsselaere 2009; Karampelas & Van Doorsselaere 2021), or random motions around footpoints of the oscillating loop (Afanasyev, Van Doorsselaere & Nakariakov 2020; Ruderman & Petrukhin 2021; Ruderman, Petrukhin & Pelinovsky 2021). Apparently decayless patterns could also appear because of the development of the Kelvin–Helmholtz instability (e.g. Antolin et al. 2016; Guo et al. 2019).

The recent commissioning of the High Resolution Imager (HRI) of the Extreme Ultraviolet Imager (EUI; Rochus et al. 2020), onboard *Solar Orbiter* (Müller et al. 2020), opens up interesting perspectives in the high-resolution study of the decayless kink oscillation phenomenon. This extends beyond the resolution of the Atmospheric Imaging Assembly (AIA; Lemen et al. 2012) on the *Solar Dynamics Observatory* (*SDO*; Pesnell, Thompson & Chamberlin 2012), which is currently used for time–distance (TD)

★ E-mail: sihui.zhong@warwick.ac.uk (SZ); v.nakariakov@warwick.ac.uk (VMN); d.kolotkov.1@warwick.ac.uk (DYK)

analysis of these oscillations. In particular, one may anticipate to resolve higher parallel harmonics that should result naturally from a broad-band driver (e.g. Duckenfield et al. 2018; Afanasyev et al. 2020), and obtain more robust information about the variability of instantaneous parameters of the oscillation (e.g. Zhong et al. 2022) and the oscillating loops (e.g. Karampelas et al. 2019; Shi et al. 2021).

In this paper, we present the simultaneous detection of decayless kink oscillations with HRI and AIA, which has been successfully used for the observations of decayless kink oscillations for almost 10 yr. The oscillation periods detected in this study vary from 1 to 3 min, which is in the short limit of the previous detections by AIA. We consider this study as the necessary step towards the follow-up progression to shorter time-scales detected by HRI, which are not possible with AIA.

2 OBSERVATIONS AND DATA ANALYSIS

A series of 174 Å images was obtained with HRI from 22:58 UT on 2021 November 5 to 00:28 UT on 2021 November 6. The field of view (FOV) was 2048 × 2048 pixels with the pixel size of 0.492 arcsec and the time cadence of 5 s. In this study, we use Level 2 data.[1] The HRI telescope was pointed at near the disc centre, where a bundle of loops with ongoing decayless kink oscillations was situated at an active region. Simultaneous observation was acquired by *SDO*/AIA at 171 Å with a pixel size of 0.6 arcsec and time cadence of 12 s. At the time of observation, the *Solar Orbiter* was at a distance of 0.86 au from the Sun, at the Stonyhurst heliographic longitude of −0.°574, and the latitude of 1.°987, while *SDO* was at a distance of 0.99 au, longitude of −0.°0129, latitude of 3.°875. In this case, see Fig. 1, both spacecrafts have nearly parallel lines of sight (LOS). Also, such a location determines the linear plate scale of HRI images as 306 km pixel^{-1}, while that of AIA images is 435 km pixel^{-1}. With higher spatial resolution and double temporal resolution, HRI allows us to detect short-period low-amplitude kink oscillations of plasma structures, but our aim is to study the oscillation detected simultaneously by both HRI and AIA. We select a similar 171 Å wavelength in AIA in comparison with HRI 174 Å to confirm the oscillation detection. In addition, magnetograms from the Helioseismic and Magnetic Imager (HMI; Scherrer et al. 2012), with resolution of 0.5 arcsec pixel^{-1} and cadence of 45 s, are used to establish the magnetic connectivity of the loops of interest.

2.1 Alignment

After compensating the solar rotation in all data sets, it is found that the pointing accuracy of HRI images as defined in the image metadata (FITS keywords) is not sufficient for this study. So the HRI images need to be internally aligned to remove spacecraft jitter.

One frequently used method to do image alignment is the cross-correlation technique (Zitová & Flusser 2003). This method first calculates the cross-power spectrum of the reference image and aligned image, and returns a cross-correlation surface/matrix of the same size as the image through the inverse Fourier transform. The distance from the location of the maximum correlation to the surface centre in Cartesian axes is the offset in the x and y directions. Given that the correlation matrix is in units of pixels, the location of the maximum value is in a certain pixel.

[1]The EUI L2 data we used can be accessed via 'EUI Data Release 5.0 2022-04', see https://doi.org/10.24414/2qfw-tr95.

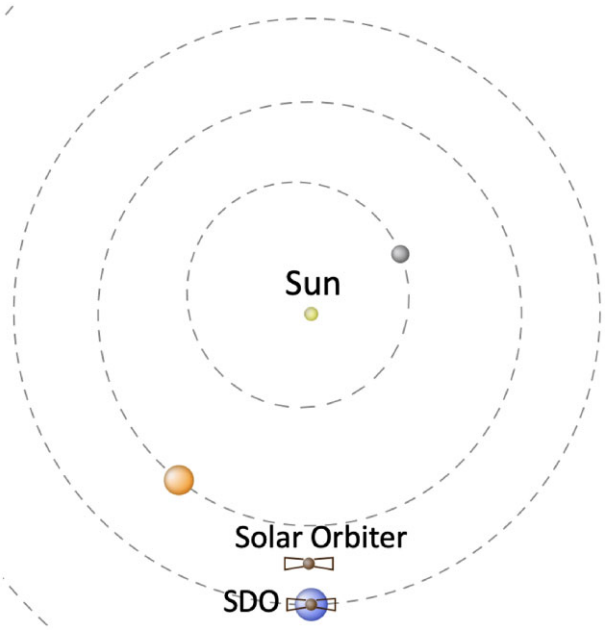

Figure 1. The locations of *Solar Orbiter* and *SDO* at 22:58 UT on 2021 November 5, seen in the ecliptic plane. The grey, orange, and blue circles with dashed orbit are Mercury, Venus, and Earth, respectively. This is a screenshot from the propagation tool (http://propagationtool.cdpp.eu/).

To achieve the sub-pixel accuracy, we interpolate the correlation peak (Lehmann, Gonner & Spitzer 1999). The corresponding SSWIDL function is `tr_get_disp.pro`, which is the core block for the later developed routines `align_cube_correl.pro` and `fg_rigidalign.pro`. The accuracy of `fg_rigidalign.pro` is several tenths of a pixel, see https://hesperia.gsfc.nasa.gov/ssw/trace/idl/util/tr_get_disp.pro. Alternatively, upsampling the correlation surface can also result in sub-pixel accuracy (e.g. Guizar-Sicairos, Thurman & Fienup 2008; Almonacid-Caballer, Pardo-Pascual & Ruiz 2017).

Recently, Feng et al. (2012) developed an algorithm to locate the correlation peak with high accuracy by treating the centroid of the correlation surface as the peak. This algorithm first calculates the displacement of the pixel level and shifts the aligned image, then it performs iteration of the offset calculation and shifting until the displacement is less than 1 pixel, finally locates the centroid with accuracy as high as 0.01 pixel (i.e. 36 km in the analysed data, i.e. 1/5 of average amplitude of decayless oscillations 170 km) and shifts the sub-pixel displacement (Yang et al. 2015). Considering its high accuracy, we apply this method to align the HRI data in this study.

2.2 Coalignment and motion magnification

After the internal alignment, coalignment between HRI images and AIA images closest in time is performed based on the common features in both data sets. HMI data are already aligned with AIA. For further analysis, subframes are extracted at the same FOV (indicated by the red box in Fig. 2b) and stacked into a 3D data cube, respectively.

At 22:58 UT on 2021 November 5, the HRI telescope captures a scene near the disc centre, including active region (AR) 12983 with several bundles of loops evolving. During this 1.5-h observation, decayless kink oscillations of an ensemble of loops are observed, and no flares or coronal mass ejections (CMEs) are reported in this

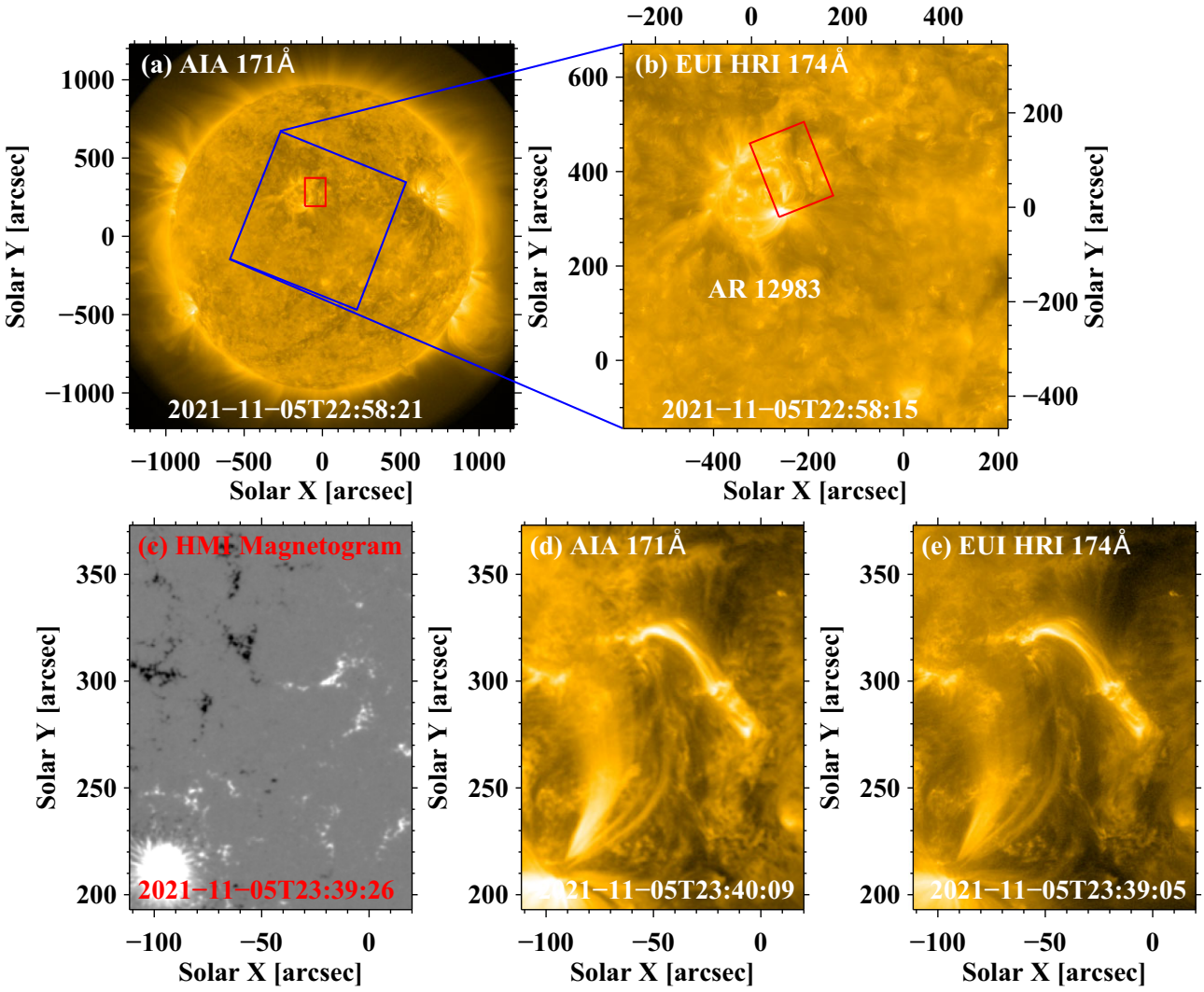

Figure 2. Panel (a): full-disc image in the AIA 171 Å passband. Panel (b): HRI 174 Å image, whose field of view (FOV) is overplotted on panel (a) as the blue box. Bottom panels: HMI magnetogram, AIA 171 Å image, and an HRI image extracted in the FOV of interest. All three images are aligned. The FOV of HRI images is overplotted on the full-disc 171 Å image. The red rectangles in panels (a) and (b) indicate the FOV of interest.

region. A similar scene is simultaneously recorded by AIA. As the characteristic displacement amplitude (0.17 Mm) of decayless kink oscillations is less than the pixel size of both data sets, we use the motion magnification technique to magnify the transverse motions in the plane of the sky (Anfinogentov & Nakariakov 2016; Zhong et al. 2021). In this work, the magnification factor is 3, and smoothing width is 4 min, which is longer than the oscillation periods of interest. Having applied the motion magnification to HRI and AIA data sets, we make TD plots (Fig. 4) using slits (see white slits in Fig. 3) directed across the oscillating loops, to reveal the oscillatory patterns (see Zhong et al. 2022, for the methodological details).

3 RESULTS

3.1 Oscillation detection

Fig. 2 shows the full-disc AIA 171 Å image (panel a) and HRI 174 Å image (panel b) obtained at the beginning of the observation. The FOV of HRI is indicated by the blue box, and the red rectangles indicate the FOV of panels (c)–(e), which is the region of interest where the oscillations occur. The bottom panels of Fig. 2 display the HMI magnetogram (panel c), AIA 171 Å image (panel d), and HRI 174 Å image (panel e), all of which are aligned. The sunspot is situated at the bottom left-hand corner of FOV. The oscillations occur in the bright loops near [−50 arcsec, 320 arcsec], connecting two small magnetic patches of opposite polarities. The apparent distance between the loop footpoints is 32 Mm, hence the loop length is estimated as $L = \pi \times 32/2 = 51 \pm 16$ Mm, assuming that the loop shape is semicircular. See also the online animation that shows the coaligned HRI 174 Å images (left) and AIA 171 Å images (right) with time corrected.

The bundle of loops that hosts oscillations is shown in Fig. 3. The images of upper and bottom rows are made with HRI and AIA, respectively. Besides the obvious difference in image quality and despite the slightly different bandpasses, the images appear very similar. Within this bundle of loops, several distinguishable threads (denoted by the coloured arrows) evolve quickly, resulting in that the observed kink oscillations appear to be short-lived. Two slits 'S1' and 'S2' across the loops are used to make TD plots to reveal the oscillatory patterns. As shown in Fig. 4, all oscillations last for only

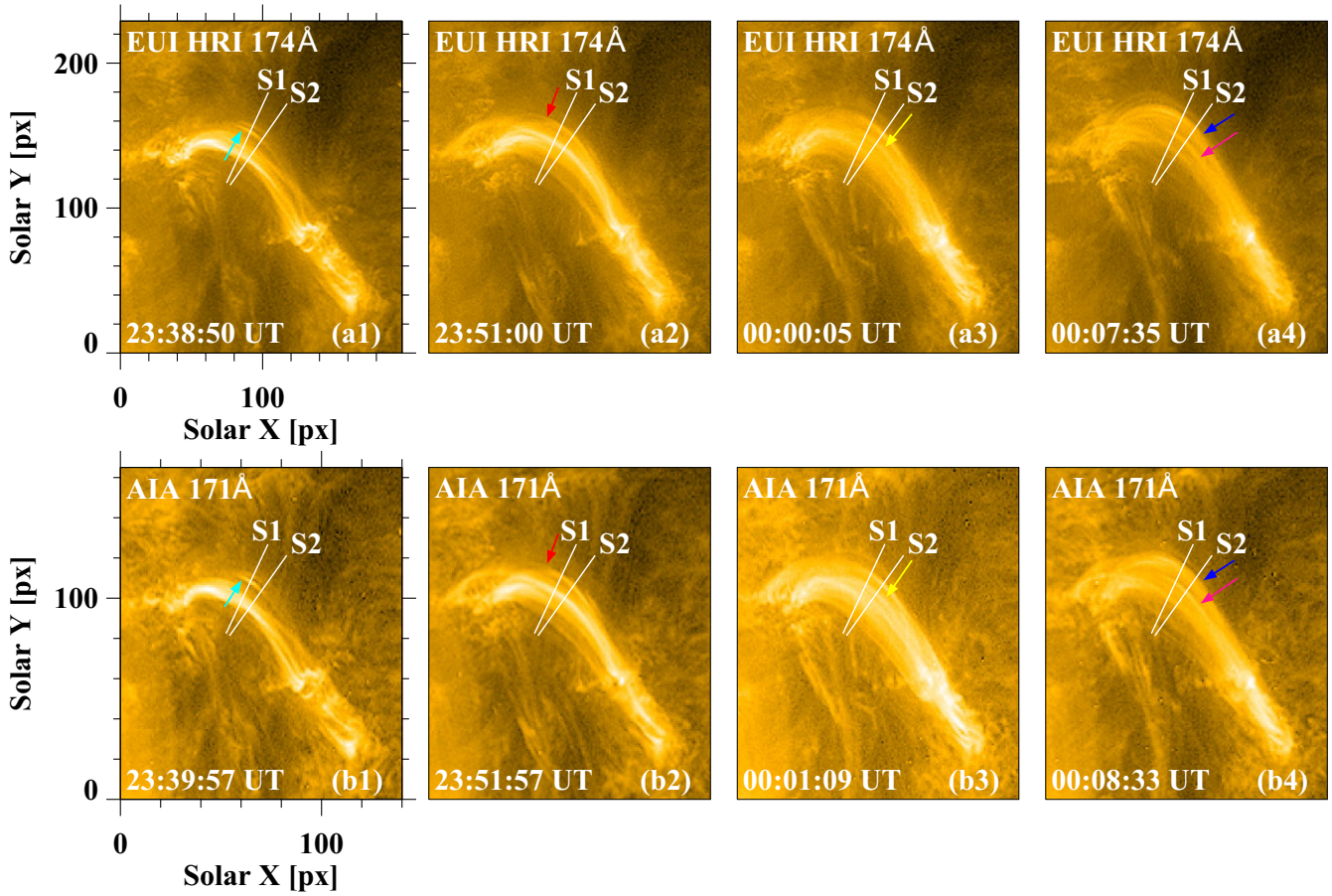

Figure 3. The dynamics of analysed threads. Slits 'S1' and 'S2' are used to make time–distance (TD) maps in Fig. 4. The coloured arrows denote the oscillating threads that have distinct oscillatory patterns. The images are enhanced to reveal the threads, by applying a high-boost mask.

several cycles, up to 15 min. The disappearance of oscillations is caused by changing of observational conditions, e.g. other loops come into the LOS, rather than damping. The oscillation signal of a certain thread is highlighted by curves of the same colour. These curves, marking the location of the loop centre or boundary at each instant of time, are determined by fitting the transverse loop profile for each instance of time with a Gaussian profile by `gaussfit.pro`.

To estimate the oscillation parameters, each oscillating signal is best fitted by a harmonic function with a linear background trend:

$$A(t) = A_0 \sin\left(\frac{2\pi t}{P} + \phi\right) + c_0 + c_1 t, \quad (1)$$

where A_0 is the displacement amplitude, P is the oscillation period, ϕ is the phase, and c_0 and c_1 are constants. The fitting results are summarized in Table 1. The details of best-fitting curves are given in Appendix A. Note that here the oscillation amplitude is linearly magnified by a factor of 3, so the original amplitude is $A = A_0/3$. For convenience, the oscillating threads are numbered in the chronological order, i.e. from Thread 1 (T1 for short) to Thread 7 (T7), corresponds to the green, cyan, red, yellow, white, blue, pink threads. The oscillation periods of T1–T7 are within 1–3 min, ranging from 67 to 133 s. Compared with the previous observed events (e.g. Anfinogentov et al. 2015; Zhong et al. 2022), the oscillation periods in this study are rather short (see Section. 3.3). In addition, displacement amplitudes vary from 24 to 83 km, which is much lower than the average amplitude of 170 km (Anfinogentov et al. 2015). Note that the values of the parameters obtained in HRI and AIA are consistent, within error bars. The averaged periods from T1 to T7 are 84 ± 21, 74 ± 9, 104 ± 11, 83 ± 16, 87 ± 9, 111 ± 33, and 108 ± 6 s, respectively. The averaged amplitudes from T1 to T7 are 34 ± 14, 41 ± 13, 71 ± 14, 59 ± 18, 35 ± 9, 63 ± 16, and 41 ± 14 km.

3.2 Correlation of oscillations in two data

Signals from HRI (see Figs 4a1 and a2) and AIA (see Figs 4b1 and b2) are very similar in shape but AIA signals are delayed by around 1 min. During the observation, the distance difference of two spacecrafts from the Sun was 1.98×10^7 km, giving the light travel time of 66 s. That is to say, the EUI received light 66 s earlier than AIA. Taken this into account, we correct the AIA signals by shifting the signal forward by 66 s. As shown in Fig. 5, the corrected AIA and HRI signals are consistent with each other, both in space and time. To quantify the correlation of the oscillations in two data, the cross-correlation coefficient between the HRI and corrected AIA signal is calculated for each thread and displayed in Table 1. The cross-correlations coefficient between signals from two data sets for T1–T7 is 0.94, 0.97, 0.92, 0.96, 0.82, 0.95, and 0.97, respectively. This indicates that oscillations seen with the two instruments correlate well with each other.

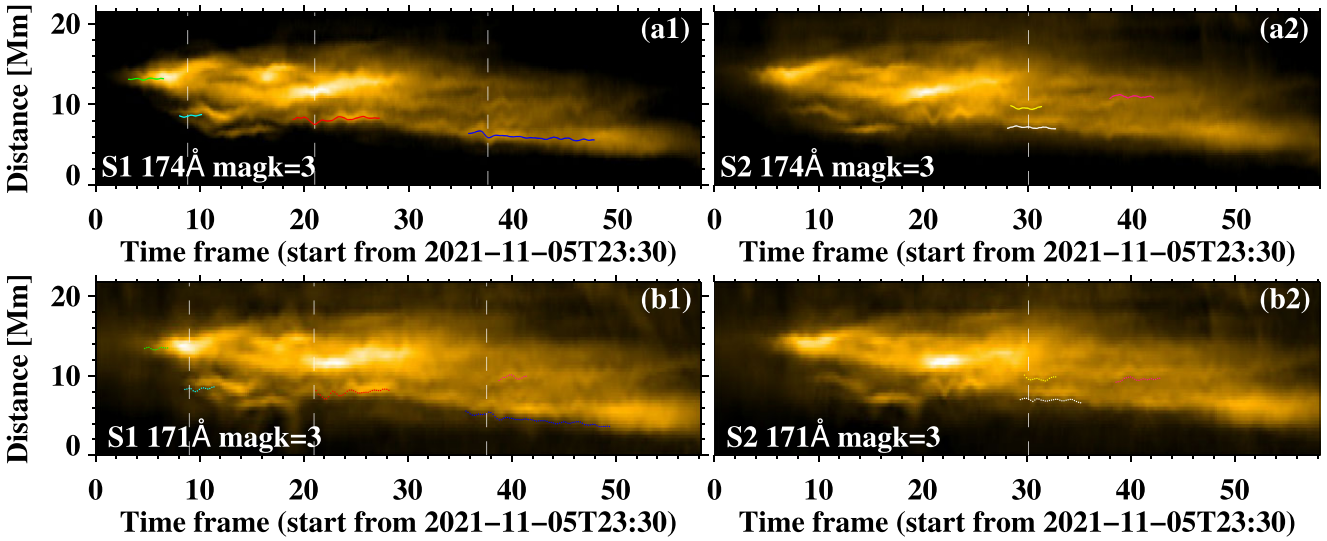

Figure 4. Time–distance (TD) maps that display decayless kink oscillations. The dashed lines denote the observation time of HRI images in Fig. 3. The coloured curves indicate the displacement location of centre/edge of corresponding oscillating threads in Fig. 3. The magnification factor is 3 for both data sets.

Table 1. Oscillation parameters of different oscillating thread estimated in HRI and AIA data. Information includes the thread ID, data source, period (P in s), displacement amplitude (A in km, the magnified amplitude divided by magnification factor, i.e. $A = A_0/3$), and cross-correlation coefficient (C) of signals from these two data sets.

Thread	Data	P (s)	A (km)	C
T1	HRI 174	76 ± 11	24 ± 7	0.94
	AIA 171	91 ± 30	45 ± 22	
T2	HRI 174	67 ± 8	28 ± 5	0.97
	AIA 171	80 ± 10	53 ± 22	
T3	HRI 174	107 ± 8	70 ± 9	0.92
	AIA 171	100 ± 13	72 ± 19	
T4	HRI 174	80 ± 8	47 ± 6	0.96
	AIA 171	86 ± 24	71 ± 30	
T5	HRI 174	83 ± 9	28 ± 5	0.82
	AIA 171	90 ± 8	42 ± 13	
T6	HRI 174	104 ± 5	31 ± 10	0.95
	AIA 171	112 ± 6	51 ± 17	
T7	HRI 174	89 ± 10	44 ± 5	0.97
	AIA 171	133 ± 55	83 ± 26	

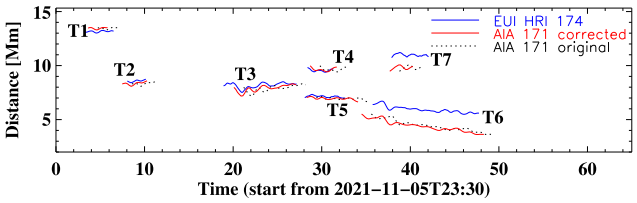

Figure 5. All oscillation signals obtained from HRI 174 Å images (blue) and AIA 171 Å images (red and black). The solid red curves are corrected signals with light traveltime difference compensation. The black dotted curves are original uncorrected signals.

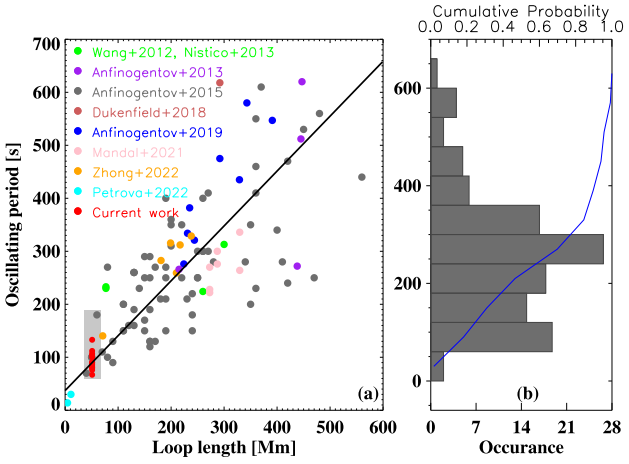

Figure 6. Scaling of the oscillation period and loop length (a) and histogram of periods (b) based on this work and previous studies on decayless kink oscillations of coronal loops. Data pairs in red are obtained in this study. The grey region in shade represents the range of parameters in this work. Data pair shown in green, purple, grey, Indian red, blue, pink, orange, and cyan are collected from Wang et al. (2012), Nisticò et al. (2013), Anfinogentov et al. (2013, 2015), Duckenfield et al. (2018), Anfinogentov & Nakariakov (2019), Mandal et al. (2021), Zhong et al. (2022), and Petrova et al. (2022), respectively. The black line is the best linear fit with the gradient of about unity. The bin size of histogram is 1 min. The blue curve is the cumulative probability. Noting that the loop lengths of the oscillating loops reported in Mandal et al. (2021) have not been provided but measured in our study.

3.3 Short periodicity

Fig. 6(a) shows the scaling of the loop length and oscillation periods obtained in this study and previous reports of decayless kink oscillations of coronal loops (e.g. Wang et al. 2012; Anfinogentov, Nisticò & Nakariakov 2013; Nisticò, Nakariakov & Verwichte 2013; Anfinogentov et al. 2015; Duckenfield et al. 2018; Anfinogentov & Nakariakov 2019; Mandal, Tian & Peter 2021; Petrova et al. 2022; Zhong et al. 2022). As mentioned in Section 3.1, the oscillation periods in our work are rather short (<3 min), so our data points

lie in the lower left-hand corner of the scaling plot. The previously established linear scaling of the loop length and period is not broken down by our results, as demonstrated by the black line, the best linear fit with the gradient of about 1.0 s Mm^{-1}.

In our observations, only certain segments near the loop top are clearly seen; see Fig. 3. Thus we cannot identify the exact locations of the footpoints of oscillating threads, and take two polarities connected by this set of loops as approximate footpoints in the length estimation. The shaded box in Fig. 6(a) indicates the uncertainty in the loop length. We need to note that the period depends also on the local kink speed, which should explain the data scattering. During the observation, the oscillating loops are evolving, hence the instantaneous local kink speed is changing too. Also, a histogram of periods overplotted with the cumulative probability is shown in Fig. 6(b).

4 DISCUSSION

Using HRI and AIA imaging data, we analyse decayless kink oscillations of several loops anchored at a quiescent active region. In similar observational channels (171 Å of AIA and 174 Å of HRI), and with almost parallel LOS, the dynamics of loops is found to be visually identical in these two data sets.

The observed oscillation signals are short-lasting, with amplitude below 0.1 Mm and periods shorter than 2 min. The AIA signals delay for 66 s compared to HRI because of different distances from the Sun. After the time correction, cross-correlation coefficients between oscillation signals in two data sets are typically higher than 0.9, suggesting oscillations recorded by two instruments are well consistent spatially and temporally. Therefore, the observed oscillations are of the physical nature.

4.1 Detection of short time-scales

The period of analysed oscillations varies from 67 to 133 s, which is rather short in comparison to previously reported cases. The uncertainties in the period estimation in Table 1 are connected with a relatively short duration of the oscillation detection (for some signals we only have a dozen of the loop displacement measurements), choice of the model to fit (the observed oscillatory signals may not be well described by a sine function), and the effects of slowly varying background, surrounding threads, and noise.

In Fig. 6(b), the number of cases with periods longer than 6 min or shorter than 3 min is 39, which is smaller than a third of the total number of 116 cases. On one hand, long periodicities (>6 min) are possibly underreported because the long loops (>400 Mm) are rare and short-lived. Moreover, the detection of oscillations requires the preferable observational conditions, e.g. the contrasted boundary of the oscillating loop, to exist for longer than three oscillation period, which is less possible for longer periods. On the other hand, short periodicities are rarely detected due to (1) the limited resolution (both temporal and spatial) of available instruments; (2) shorter loops are usually not well isolated and they evolve rapidly.

Since the period of kink oscillations scale linearly with the loop length (assuming for a certain parallel harmonics), short periodicity can be formed in the shorter loop, i.e. loop with lower height. Shorter plasma structures usually occur at the small-scale active regions (e.g. newly emerging ones) or short-distance magnetic polarity pairs. Therefore, short-period decayless kink oscillation possesses the potential for seismological diagnostics of the confined plasma at some certain coronal environments. Recently, Gao et al. (2022) reported decayless kink oscillations of loops (averaged loop length is 23 Mm) in mini-active regions, and successfully applied these oscillations to estimate Alfvén speed, magnetic field strength of the hosting loops. In addition, short periodicities are of interest for the study of higher parallel harmonics of kink oscillations, and non-linear cascade, e.g. the Kelvin–Helmholtz instability (e.g. Terradas et al. 2008; Ruderman 2017; Terradas, Magyar & Van Doorsselaere 2018).

The two-spacecraft detection of short periodicity in our work moves a step closer to unexplored regime of shorter oscillation periods, e.g. shorter than 1 min. It shows that our current methods are applicable for short-period oscillations taken with EUI data. In particular, a candidate event of short-period decayless oscillations taken by EUI was observed by Petrova et al. (2022), with oscillation periods of 14 and 30 s in two short loops of 4.5 and 11 Mm, respectively. Moreover, in addition to the discussed kink oscillations, HRI with time cadence up to 2 s could resolve such short-period wave phenomena as sausage oscillations of flare loops with period of tens of seconds (e.g. Li et al. 2020, and references therein).

4.2 The problem of alignment

HRI images are affected by the spacecraft jitter. Some of this jitter (but not all) is measured by the spacecraft itself and recorded in the metadata of the EUI images (FITS World Coordinate System keywords). For the EUI Full Sun Imager (FSI), this pointing information is further updated on the ground with a limb-fitting procedure. For the partial FOV images taken by HRI this is however not possible and only the spacecraft provided pointing information is available. Therefore additional alignments internal to the analysed data cube are needed to get rid of the remaining spacecraft jitter. For the detection of oscillations of low amplitude and short period, the accuracy of the alignment is crucial as inaccurate alignment may lead to the appearance of artificial oscillations.

As mentioned in Section 2.1, the correlation-based internal alignment could achieve sub-pixel accuracy. In practice, other factors affecting the accuracy include the selection of the correlated region (location and size), the frames correlated at one time, etc. In addition, it is found that the image enhancement prior to the alignment helps to improve accuracy (e.g. Pratt 1974; Liang et al. 2021). In the final step of alignment, 2D shifting with non-integer displacement by interpolation would degrade the spatial resolution of images. However, the loss of information is very minor. The high correlation of small-amplitude kink oscillations detected with HRI and AIA indicates that this internal alignment procedure is highly robust.

5 CONCLUSIONS

In this study, short-period decayless kink oscillations of an ensemble of loops are investigated, utilizing EUI–HRI 174 Å image sequence and coaligned AIA observation in the 171 Å channel. The analysis of imaging data is performed with the motion magnification technique. The observed oscillating loops have average length of 51 Mm, oscillation periods are about 60–100 s, and displacement amplitudes of 24–83 km. Given that EUI and AIA have different distances from the Sun, oscillations captured by AIA are delayed by 66 s. After compensation of this time lag, oscillations obtained in two data are correlated well with each other, with their cross-correlation coefficients ranging from 0.82 to 0.97. It is confirmed that EUI-HRI sees the same oscillations as AIA, a well-tested instrument, which is a starting point for progressing to the study of shorter oscillation periods with HRI.

ACKNOWLEDGEMENTS

Solar Orbiter is a mission of internal cooperation between ESA and NASA, operated by ESA. The EUI instrument was built by CSL, IAS, MPS, MSSL/UCL, PMOD/WRC, ROB, and LCF/IO with funding from the Belgian Federal Science Policy Office (BELSPO/PRODEX PEA C4000134088), the Centre National d'Etudes Spatiales (CNES), the UK Space Agency (UKSA), the Bundesministerium für Wirtschaft und Energie (BMWi) through the Deutsches Zentrum für Luft- und Raumfahrt (DLR), and the Swiss Space Office (SSO). *SDO* data supplied courtesy of the *SDO*/HMI and *SDO*/AIA consortia. SZ is supported by the China Scholarship Council–University of Warwick joint scholarship. VMN and DYK acknowledge support from the STFC Consolidated Grant ST/T000252/1.

DATA AVAILABILITY

In this paper, we analysed data using the Interactive Data Language (IDL), SolarSoftWare (SSW; Freeland & Handy 1998) package, the motion magnification technique (Anfinogentov & Nakariakov 2016), and the Solar Bayesian Analysis Toolkit (SoBAT; Anfinogentov et al. 2021). The EUI data are available at DOI: https://doi.org/10.24414/2qfw-tr95. The AIA and HMI data are available at http://jsoc.stanford.edu/. The data are processed and analysed using the routines available at https://www.lmsal.com/sdodocs/doc/dcur/SDOD0060.zip/zip/entry/ (section 7). The motion magnification code is available at https://github.com/Sergey-Anfinogentov/motion_magnification.

REFERENCES

Afanasyev A. N., Van Doorsselaere T., Nakariakov V. M., 2020, A&A, 633, L8
Almonacid-Caballer J., Pardo-Pascual J. E., Ruiz L. A., 2017, Remote Sensing, 9, 1051
Andries J., Arregui I., Goossens M., 2005, ApJ, 624, L57
Andries J., van Doorsselaere T., Roberts B., Verth G., Verwichte E., Erdélyi R., 2009, Space Sci. Rev., 149, 3
Anfinogentov S., Nakariakov V. M., 2016, Sol. Phys., 291, 3251
Anfinogentov S. A., Nakariakov V. M., 2019, ApJ, 884, L40
Anfinogentov S., Nisticò G., Nakariakov V. M., 2013, A&A, 560, A107
Anfinogentov S. A., Nakariakov V. M., Nisticò G., 2015, A&A, 583, A136
Anfinogentov S. A., Nakariakov V. M., Pascoe D. J., Goddard C. R., 2021, ApJS, 252, 11
Antolin P., De Moortel I., Van Doorsselaere T., Yokoyama T., 2016, ApJ, 830, L22
Duckenfield T., Anfinogentov S. A., Pascoe D. J., Nakariakov V. M., 2018, ApJ, 854, L5
Feng S., Deng L., Shu G., Wang F., Deng H., Ji K., 2012, in 2012 IEEE Fifth International Conference on Advanced Computational Intelligence (ICACI). IEEE, Piscataway, NJ, p. 626
Freeland S. L., Handy B. N., 1998, Sol. Phys., 182, 497
Gao Y., Tian H., Van Doorsselaere T., Chen Y., 2022, ApJ, 930, 55
Guizar-Sicairos M., Thurman S. T., Fienup J. R., 2008, Opt. Lett., 33, 156
Guo M., Van Doorsselaere T., Karampelas K., Li B., Antolin P., De Moortel I., 2019, ApJ, 870, 55
Karampelas K., Van Doorsselaere T., 2020, ApJ, 897, L35
Karampelas K., Van Doorsselaere T., 2021, ApJ, 908, L7
Karampelas K., Van Doorsselaere T., Pascoe D. J., Guo M., Antolin P., 2019, Frontiers Astron. Space Sci., 6, 38
Lehmann T., Gonner C., Spitzer K., 1999, IEEE Trans. Medical Imaging, 18, 1049
Lemen J. R. et al., 2012, Sol. Phys., 275, 17
Li B., Antolin P., Guo M. Z., Kuznetsov A. A., Pascoe D. J., Van Doorsselaere T., Vasheghani Farahani S., 2020, Space Sci. Rev., 216, 136
Liang Y., Qu Z. Q., Chen Y. J., Zhong Y., Song Z. M., Li S. Y., 2021, MNRAS, 503, 5715
Mandal S., Tian H., Peter H., 2021, A&A, 652, L3
Müller D. et al., 2020, A&A, 642, A1
Nakariakov V. M., Aschwanden M. J., van Doorsselaere T., 2009, A&A, 502, 661
Nakariakov V. M., Anfinogentov S. A., Nisticò G., Lee D. H., 2016, A&A, 591, L5
Nakariakov V. M. et al., 2021, Space Sci. Rev., 217, 73
Nisticò G., Nakariakov V. M., Verwichte E., 2013, A&A, 552, A57
Pesnell W. D., Thompson B. J., Chamberlin P. C., 2012, Sol. Phys., 275, 3
Petrova E., Magyar N., Van Doorsselaere T., Berghmans D., 2022, preprint (arXiv:2205.05319)
Pratt W. K., 1974, IEEE Trans. Aerospace Electron. Syst., AES-10, 353
Rochus P. et al., 2020, A&A, 642, A8
Ruderman M. S., 2017, Sol. Phys., 292, 111
Ruderman M. S., Petrukhin N. S., 2021, MNRAS, 501, 3017
Ruderman M. S., Petrukhin N. S., Pelinovsky E., 2021, Sol. Phys., 296, 124
Scherrer P. H. et al., 2012, Sol. Phys., 275, 207
Shi M., Van Doorsselaere T., Antolin P., Li B., 2021, ApJ, 922, 60
Terradas J., Andries J., Goossens M., Arregui I., Oliver R., Ballester J. L., 2008, ApJ, 687, L115
Terradas J., Magyar N., Van Doorsselaere T., 2018, ApJ, 853, 35
Tian H., McIntosh S. W., Wang T., Ofman L., De Pontieu B., Innes D. E., Peter H., 2012, ApJ, 759, 144
Van Doorsselaere T. et al., 2020, Space Sci. Rev., 216, 140
Wang T., Ofman L., Davila J. M., Su Y., 2012, ApJ, 751, L27
Yang Y.-F., Qu H.-X., Ji K.-F., Feng S., Deng H., Lin J.-B., Wang F., 2015, Res. Astron. Astrophys., 15, 569
Zhong S., Duckenfield T. J., Nakariakov V. M., Anfinogentov S. A., 2021, Sol. Phys., 296, 135
Zhong S., Nakariakov V. M., Kolotkov D. Y., Anfinogentov S. A., 2022, MNRAS, 513, 1834
Zitová B., Flusser J., 2003, Image Vision Comput., 21, 977

SUPPORTING INFORMATION

Supplementary data are available at *MNRAS* online.

raw_174vs171_corrected_1080p.mp4

Please note: Oxford University Press is not responsible for the content or functionality of any supporting materials supplied by the authors. Any queries (other than missing material) should be directed to the corresponding author for the article.

APPENDIX A: CURVE FITTING

Here we demonstrate the best sinusoidal fits of the oscillation signals of T1–T7 obtained in the HRI and AIA data. The signals (see the red dots in Fig. A1) are best fitted with equation (1) to estimate the oscillation period and displacement amplitude, using the Markov chain Monte Carlo method (Anfinogentov et al. 2021; the algorithm is available at https://github.com/Sergey-Anfinogentov/SoBAT). The best-fitting parameters are shown in Table 1 and the best-fitting curves are represented by the solid curves in Fig. A1.

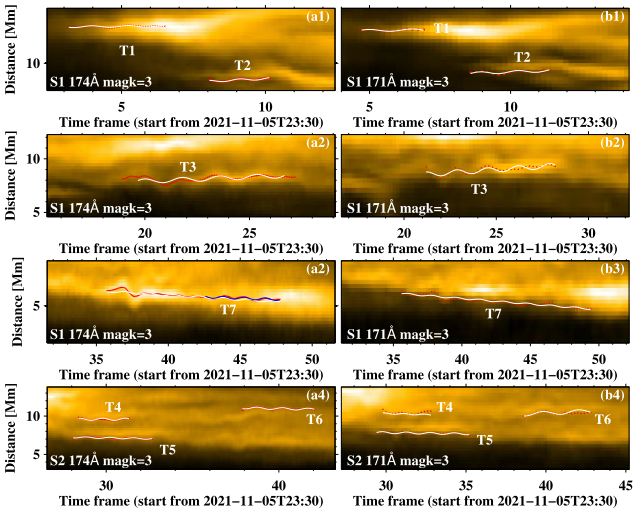

Figure A1. The analysed oscillation signals (red dots) obtained by HRI (a1)–(a2) and AIA (b1)–(b4) and their corresponding best sine fits (solid curves).

This paper has been typeset from a TEX/LATEX file prepared by the author.